American Mineralogist, Volume 102, pages 135–148, 2017

An experimental kinetic study on the structural evolution of natural carbonaceous material to graphite

YOSHIHIRO NAKAMURA[1,*], TAKASHI YOSHINO[2], AND MADHUSOODHAN SATISH-KUMAR[3]

[1]Graduate School of Science and Technology, Niigata University, 2-8050 Ikarashi, Nishi-ku, Niigata 950-2181, Japan
[2]Institute for Planetary Materials, Okayama University, Misasa, Tottori 682-0193, Japan
[3]Department of Geology, Faculty of Science, Niigata University, 2-8050 Ikarashi, Nishi-ku, Niigata 950-2181, Japan

ABSTRACT

We report here new experimental kinetic data on the structural evolution of carbonaceous material (CM) to graphite during heating at various temperatures (1000 to 1450 °C) for various durations (10 min to 115 h) under a pressure of 1 GPa. Natural CMs extracted from sedimentary rocks in the Shimanto accretionary complex and the Hidaka metamorphic belt of Japan transformed in morphology and crystallinity with increasing temperature and annealing duration to become fully ordered graphite (d_{002} spacing ~3.36 Å). Transmission electron microscopy showed that both samples have undergone microstructural evolution from amorphous carbon to platy graphitic carbon. These changes match the evolution of the samples' X-ray diffraction (XRD) patterns and micro-Raman spectra. The time–temperature relations of crystal parameters obtained by XRD and micro-Raman spectroscopy demonstrated a sigmoidal transformation curve from an amorphous to a graphitic structure, suggesting complexity of these successive and/or parallel chemical reactions are responsible for graphitization. To assess these complex chemical processes, we adopted three different approaches for formulating the graphitization kinetics using a power rate model, a Johnson-Mehl-Avrami (JMA) model and a superposition method. Irrespective of the models employed, the effective activation energies were estimated to lie between 259 and 339 kJ/mol, which are much lower than those reported previously for graphitization. Summarizing the previous studies and our results between 0.1 and 1000 MPa, we found that the effective activation energies systematically decrease as a function of pressure. Based on the experimental results in this study, the sigmoid functions obtained from the time–temperature relations can be extrapolated to low-temperature conditions at 1 GPa. Our kinetic model using unit-cell height *c* predicts that CM undergoing metamorphism for about 1 m.y. will begin to crystallize at ~410 °C, and will transform to fully ordered graphite at over ~520 °C. Thus, natural graphitization undergoes a much faster transformation than reported in previous studies at 1 atm and could be explored in laboratory experiments using natural precursor materials under pressure conditions and time spans that reflect natural conditions in the Earth's crust.

Keywords: Graphitization, carbonaceous material, kinetic model, HPHT experiment

INTRODUCTION

Carbonaceous material (CM) is a widespread accessory phase in sediments, and its composition and structure are sensitive to change during metamorphism (Buseck and Beyssac 2014). The structural evolution of CM to graphite is one of the most important thermal indicators for geological regimes of low to medium metamorphic temperatures and is widely used as a geothermometer (Beyssac et al. 2002; Kouketsu et al. 2014). However, the process sensu stricto is not a simple recrystallization that depends only on metamorphic temperature. The organic precursor materials of CM in sediments have complex supramolecular structures (Oberlin et al. 1999; Schwab et al. 2005), and their evolutions in chemical composition, microstructure, and crystallinity depend not only on thermal maturation but also on tectonic deformation, catalytic effects, and fluid activity under lithostatic pressure (Luque et al. 1998). Such complex transformations during the transition of organic matter to graphite make it difficult to understand the natural structural evolution of CM, and proper assessments of these factors during graphitization have been seldom achieved. Therefore, it is essential to consider a fundamental kinetic model for natural graphitization under geological timescales and crustal temperatures.

The natural structural evolution of organic matter to CM, and then into graphite, mainly comprises two prominent processes: carbonization and graphitization (Oberlin 1984). The early stage of carbonization begins with softening and the release of aliphatic compounds and heteroatoms with increasing temperature. After degradation of aliphatic CH groups, solid-state reorganization (the formation of basic structure units, BSUs) progresses with the release of non-condensable gases (e.g., CH_4 and H_2) from the aromatic CH groups (Oberlin et al. 1999). The BSU is the minimum structural unit of the CM nanostructure. The aggregate is stacked in two or three polyaromatic layers and acts as a nucleus for the transformation of turbostratic to a graphitic structure (Oberlin 1984; Oberlin et al. 1999). The natural and experimental kinetic approaches on carbonization have been widely investigated using vitrinite reflectance (Hood et al. 1975; Burnham and Sweeney

* E-mail: f14n002a@mail.cc.niigata-u.ac.jp

0003-004X/17/0001–135$05.00/DOI: http://dx.doi.org/10.2138/am-2017-5733

1989; Sweeney and Burnham 1990; Huang 1996), biomarker thermal maturity (Sheppard et al. 2015), carbon X-ray absorption near-edge structure spectroscopy (C-XANES: Cody et al. 2008), micro-Raman spectroscopy (Muirhead et al. 2012), and in situ micro-Fourier transform infrared spectroscopy (Kebukawa et al. 2010). These kinetic studies have reported wide ranges of apparent activation energies between 98 and 345 kJ/mol (Marsh et al. 1999), some of which are comparable to the dissociation energies of C–H bonds (346–421 kJ/mol) and C–C bonds (254–346 kJ/mol). The other major process, graphitization, involves crystallization from a turbostratic to a graphitic structure by the reorganization of stacking sheets. The structural change of CM to graphite has been well studied using X-ray diffraction (Grew 1974; Wada et al. 1994), transmission electron microscopy (Buseck and Huang 1985), and micro-Raman spectroscopy (Wopenka and Pasteris 1993). On the other hand, the experimental studies on the kinetics of graphitization are scarce in the literature. The biggest drawback in synthesizing graphite is that it requires very high treatment temperature (~3000 K) in a low f_{O_2} environment under ambient pressure. Early kinetic studies in the 1960s–1970s already reported an effective activation energy of ~1000 kJ/mol for the formation of graphite (e.g., Fischbach 1963, 1971; Murty et al. 1969). These values are in good agreement with activation energies of vacancy diffusion from experiments with natural graphite (Kanter 1957) and first-principles calculation (Kaxiras and Pandey 1988). However, such a high effective activation energy based on experimental results points to notable differences between natural and experimental structural evolution of CM. For instance, extrapolation based on previous experimental kinetic data at 1 atm suggests that even at 700 °C, graphite would require durations of the order 10^{40} min (~1.9×10^{34} years; Fischbach 1971; Bustin et al. 1995). Therefore, it is required that we should provide more realistic experimental kinetic model and more realistically constrained experimental data to understand the kinetics behind natural graphitization.

The large divergence between experimental and natural graphitization results from neglecting other factors such as lithostatic pressure (Noda et al. 1968; Beyssac et al. 2003), tectonic deformation (Ross and Bustin 1990; Bustin et al. 1995), and catalytic effects (Marsh et al. 1983). This work constructs a revised kinetic model for natural graphitization through an experimental exploration of the synthesis of graphite under relatively low temperature and pressure conditions (1000–1450 °C and 1 GPa), when compared with early kinetic studies. Previous studies on the synthesis of graphite have noted that the structural evolution of CM to graphite depends greatly on the nanostructure of the precursor materials (graphitizing and non-graphitizing carbon) (Oberlin 1984; Oberlin et al. 2006). Therefore, we used two different CM samples extracted from representative pelitic rocks in a low-grade metamorphic terrain and an accretionary complex to compare the influence of the nanostructure of the precursor. Our findings lead to a revised kinetic model for the natural structural evolution of CM, which advances our understanding of graphitization in natural environments over geological timescales. The acronyms are described in Table 1.

TABLE 1. Summary of acronyms

Acronym	Meaning
CM	Carbonaceous material
HMB	Hidaka Metamorphic Belt
SM	Shimanto accretionary complex
R1	Intensity ratio of (D1/G) bands in Raman spectroscopy
R2	Area ratio of D1/(D2+D3+G) bands in Raman spectroscopy
AR	Area ratio of (D1+D4)/(D2+D3+G) bands in Raman spectroscopy
d_{002}	Interlayer spacing of (002) in graphitic structure
FWHM	Full-width at half maximum
L_c (002)	Crystal thickness of graphite along *c*-axis
L_a	Lateral extent of carbon sheets
SAED	Selected-area diffraction pattern
BSU	Basic structure unit
JMA	Johnson-Mehl Avrami model

METHODS

Starting materials

The natural CMs in pelitic rocks are complex aggregates of two CM end-members (non-graphitizing and graphitizing carbon; Oberlin 1984). The heterogeneity of nanostructures is one of the most important factors to discuss in the recrystallization during the high-pressure high-temperature (HPHT) experiments. It is difficult to quantify the heterogeneity of nanostructures in transmission electron microscopy observations and reconstruct the natural heterogeneity of CM using the two end-members. Therefore, the starting materials for the HPHT experiments were prepared from two different naturally occurring sedimentary rocks: one from the Hidaka metamorphic belt (HMB) and the other from the Cretaceous Shimanto accretionary complex (SM). Both starting materials extracted by HF-HCl treatments were expected to demonstrate behavior closer to that in nature than observed in previous experiments using cokes and other commercial carbon materials, and especially suitable starting materials, because their localities have been well studied in terms of structural geology, metamorphic geology, and organic geochemistry (Nakamura et al. 2015; Ohmori et al. 1997).

The CM in HMB were sampled from muscovite-chlorite grade metasediments, which are located near to the boundary of the biotite isograd (see Nakamura et al. 2015 for detailed geological relations). Under the microscope, the CM was observed along the grain boundaries of quartz or plagioclase within pelitic layers, and along cleavage planes in chlorite and muscovite. The CM showed a turbostratic (sample HMB, d_{002} spacing = 3.431 ± 0.007 Å) structure in XRD profiles and high R2 ratio (R2 ratio = 0.62 ± 0.01) in micro-Raman spectroscopy.

The CM in SM were sampled from mudstone in the Hinotani unit of the Cretaceous Shimanto accretionary complex. The Hinotani unit is dominated by coherent turbidite units containing massive and bedded sandstone, interbedded sandstone and mudstone, and mudstone. The CMs in this area show the lowest maturity and systematically change their crystallinity with increasing the paleo-thermal gradient toward the out-of-sequence thrusts (Fukase fault and Aki Tectonic line), ranging between 1.3 and 3.0% of vitrinite reflectance (Ohmori et al. 1997). In addition, these sediments are considered as a candidate precursor for high-pressure metamorphic rocks such as Sambagawa metamorphic belt (e.g., Aoki et al. 2011; low-temperature, high-pressure type metamorphic terrain). Therefore, these rocks have another benefit, to compare different geothermal gradients in metamorphic regimes. Under the microscope, the CM was identified optically as two different macerals (vitrinite and inertinite), and it coexists with illite, plagioclase, quartz, and framboidal pyrite in pelitic layers. The CM showed an amorphous (sample SM, d_{002} spacing = 3.505 ± 0.013 Å) structure in XRD profiles and a broad D1 band FWHM in micro-Raman spectroscopy (D1 band FWHM = 129.4 ± 8.4 cm^{-1}). The two samples we have selected cover a wide range of crystallinity, and are suitable for applying experimental graphitization of natural CM back to the temperature–time scale of metamorphic rocks.

Chemical extraction from pelitic rocks

Given that the sedimentary rocks have low concentrations of organic carbon (total organic carbon values of 0.3–0.7 wt%; Nakamura et al. 2015), we followed the chemical extraction for preparing the required aliquots of CM samples (Nakamura and Akai 2013). The presence of silicate or oxide minerals in the starting materials may form various carbides at high temperature (>900 °C; e.g., Charon et al. 2014), therefore it is important to eliminate these minerals as much as possible by chemical extraction.

The rock samples (500–800 g) were crushed by a Jaw crusher and sieved using a 200-mesh screen. The sieved powder was initially treated with 2 N HCl to remove carbonate, sulfide, sulfate, and hydroxides (Vandenbroucke and Largeau 2007), and then the solution was treated by HF (48%) in several large polytetrafluoroethylene vessels (500 mL) and dried on a hot plate at 120 °C. Dried residues in polytetrafluoroethylene vessels were composed of CMs and newly formed fluorides such as ralstonite and other complex fluorides (Durand and Nicaise 1980). These fluorides are difficult to redissolve once precipitated and they interfere with further analysis of

CM (Vandenbroucke and Largeau 2007), therefore, we performed repeated rinsing with hot deionized water between acid treatments (Durand and Nicaise 1980). The residues were dissolved again in 2 N HCl at 60 °C. The chemical treatments were repeated several times until the CM floated in the solution. This floatation is a signal of the complete decomposition of fluorides (Itaya 1981, 1985). The supernatant of CM was filtered and dried on a watch glass. Note that the CM residues retained small amounts of minerals such as zircon, rutile, ilmenite, and pyrite even after HF–HCl acid treatments. Both starting materials of SM and HMB are slightly matured or metamorphosed during diagenesis and low-grade metamorphism, respectively. Many researchers have concluded that the HF–HCl acid treatments do not alter the CM structure and do not generate newly formed solvent soluble organic materials except in the case of very immature sediments (Durand and Nicaise 1980; Larsen et al. 1989; Vandenbroucke and Largeau 2007).

HPHT experiments

HPHT experiments were performed at the Institute for Planetary Materials (IPM), Okayama University, Misasa, Japan. The two starting materials were encapsulated and stamped in platinum tubes of 2.0 and 3.0 mm outer diameter. Experiments were carried out with both starting materials together in a single run so as to reduce any apparent difference in absolute temperature conditions. After welding and encapsulating, the platinum capsules were placed in two different pressure apparatus for appropriate treatment of temperature and time: (1) the piston-cylinder (PC) apparatus and (2) the DIA-type apparatus (AMAGAEL). For the PC experiments, the assembly was composed of a talc-borosilicate glass-graphite furnace with MgO disks as pressure medium [19.05 mm (¾″ diameter)]. Two platinum capsules were placed at the center of graphite heater. Experimental temperature was measured by type S (Pt-Pt_{90}-Re_{10}) thermocouples. For experiments using the DIA-type apparatus, the cubic pyrophyllite with edge length of 21 mm was adopted as pressure medium and the tungsten carbide anvils with top edge length was 15 mm. Temperature was monitored using $W_{97}Re_3$-$W_{75}Re_{25}$ thermocouples with Al_2O_3 insulating sleeves, whose junction was placed in contact with the center of MgO disk. We used DIA-type apparatus for high-temperature conditions (1325 and 1450 °C). Previous studies on HPHT experiments already reported that the conversion of graphite at 1 GPa required at least 1200 °C for 100 h (Beyssac et al. 2003). Therefore, our experiments were carried out at four different temperature conditions between 1000 and 1450 °C, and different annealing durations at peak temperature from 10 min to 115 h. Short experiments of 1 s duration (PC 481 and PC 482) were also carried out for reference, however, these were not used for kinetic analysis due to uncertainties in time–temperature estimates. Both experiments were carried out with a heating rate of about 100 °C/min and quenching by switching off the furnace power.

Analytical methods

The recovered platinum capsules were mounted into epoxy resin and cut into two halves. One half was used for SEM observations and micro-Raman spectroscopy. The other half was separated from the slab section of platinum capsule using a dentist diamond cutter under a binocular microscope. The powder was used for X-ray diffraction and transmission electron microscopy observations.

X-ray diffraction (XRD) was obtained using a Rigaku ULTIMA IV diffractometer at Niigata University, equipped with Cu$K\alpha$ (40 kV, 40 mA) radiation, graphite monochromator, slit system 2/3°–0.45 mm–2/3° and time constant of 0.5° min^{-1}. The diffractometer was run between 10° and 90°. The powdered samples of CM were dried on a Si-low background sample holder with internal standard of silicon (10–20 wt%). Lattice constant and crystal thickness of graphite were calculated according to the following methods. The 2θ values of the obtained peaks were calibrated using the peak positions of the internal silicon standard (Iwashita et al. 2004). The $L_c(002)$ was calculated using the Scherrer equation: $L_c(002) = K\lambda/\beta\cos\theta$, where K, constant (1.0); λ, X-ray wavelength (Cu$K\alpha$ = 1.5419 Å); β, full-width at half maximum (FWHM); θ, the Bragg angle. The K value is not a constant, but depends on the crystallite sizes (Fujimoto 2003). Therefore, we used the constant K of 1.0 for $L_c(002)$ following JIS standards (Iwashita et al. 2004).

Micro-Raman spectroscopy was applied to CM and graphite in the first-order region using a Jasco NRS 3100 spectrometer at Niigata University, equipped with the grating of 1800 lines/mm and CCD-detector (256 × 1024 pixels). The microscope objective of 100×, and Nd-YAG laser (wavelength: 532 nm) were used. Acquisition time is 10–30 s, and 3–6 spectra were cumulated for each data point. All Raman peak profiles were analyzed by using peak profile fitting, and G (1580 cm^{-1}), D1 (1350 cm^{-1}), D2 (1620 cm^{-1}), D3 (at around 1450 cm^{-1}), and D4 (at around 1200 cm^{-1}) bands in the first-order region (1000–1800 cm^{-1}) were separated. The parameters of G band FWHM, D1 band FWHM, G position (Raman shift), $R1$ ratio ($Intensity_{D1\ band}/Intensity_{G\ band}$), R2 ratio ($Area_{D1\ band}/Area_{G+D1+D2\ bands}$), and Area ratio (AR; $Area_{D1+D4\ bands}/Area_{G+D2+D3\ bands}$) were estimated. The Tuinstra and Koenig equation were applied: $I_{D1}/I_G = C(\lambda)/L_a$ (nm) (Tuinstra and Koenig 1970); where C (λ), constant (4.4); I_{D1}/I_G, $Intensity_{D1\ band}/Intensity_{G\ band}$, $R1$ ratio; L_a (nm), the crystal size of lateral extent of carbon sheets. Mean values and standard deviations were calculated based on 11–20 analyses for both edge and center part of samples.

Scanning electron microscopic (SEM) observations were carried out using a JEOL 6510LA, equipped with an energy-dispersive X-ray spectrometer (EDS) at Niigata University. Both samples were observed without coating under low vacuum pressure.

Transmission electron microscopy (TEM) was carried out using a JEOL JEM 2010 electron microscope in Niigata University, operating at 200 kV with LaB_6 filament. CM samples extracted from the run products were ground and suspended in pure water. After ultrasonic cleaning in plastic tubes, the solution was deposited on the carbon-coated holey film of the TEM micro-grid treated by plasma cleaning. The samples were mainly observed for the d_{002} lattice fringe along the [010] direction.

Results

Morphological characteristics of run products

Both CM samples show gradually changing surface optical properties (i.e., relative reflectance) as annealing occurs at increasing temperatures and for longer durations. Short annealing (1 s to 10 min) leads to the formation of many voids and cracks of 1–10 μm width in some areas of the run products (Fig. 1a). Such pores are rare in the HMB samples (Fig. 1b). Previous studies have also reported the presence of voids or porous structures on polished coal surfaces, suggesting the release of volatile matter from the precursor (Rodrigues et al. 2011; Zhou et al. 2014). Our observations also suggest a change in the bulk density of the CM due to the release of volatile matter during carbonization (Inagaki and Meyer 1999). In addition, the morphological characteristics of the CM gradually change in response to both annealing duration and temperature. Treatment at 1000 °C leads to CM samples consisting of small grains of 1–10 μm diameter with porous structures observable by SEM (Fig. 1c). Treatment at higher temperatures changes the CM to aggregates with planar structures (Fig. 1d), which do not show the hexagonal morphology commonly seen by SEM in well crystallized graphite.

XRD analysis

Both CM samples extracted from Pt capsules show systematically changing XRD profiles with respect to temperature and duration (Fig. 2a; Table 2). Crystal parameters derived from the XRD patterns reveal the evolution of three types of microstructure: amorphous (1D), turbostratic (2D), and graphitic (3D) structures. At the early stage (1 s to 10 min), SM shows a broad and symmetric reflection at the 2θ range of 40–45° in XRD profiles. This single broad reflection (named as 10 reflection) is a composite of d_{100} and d_{101} reflections, suggesting the presence of randomly oriented small stacks in amorphous structure. Longer annealing (1 to 6 h, Fig. 2a) makes the broad peaks asymmetric owing to the formation of turbostratic structure. This asymmetric peak starts to split into the d_{100} and d_{101} reflections with increasing temperature and time. The d_{112} and d_{006} reflections also appear, suggesting the formation of a graphitic structure (Fig. 2a). Both samples show such progressive structural changes from amorphous to graphitic with increasing temperature.

Micro-Raman spectroscopy

Two prominent bands corresponding to the G band (1580 cm^{-1}) and D1 band (1350 cm^{-1}) appear in the first-order region

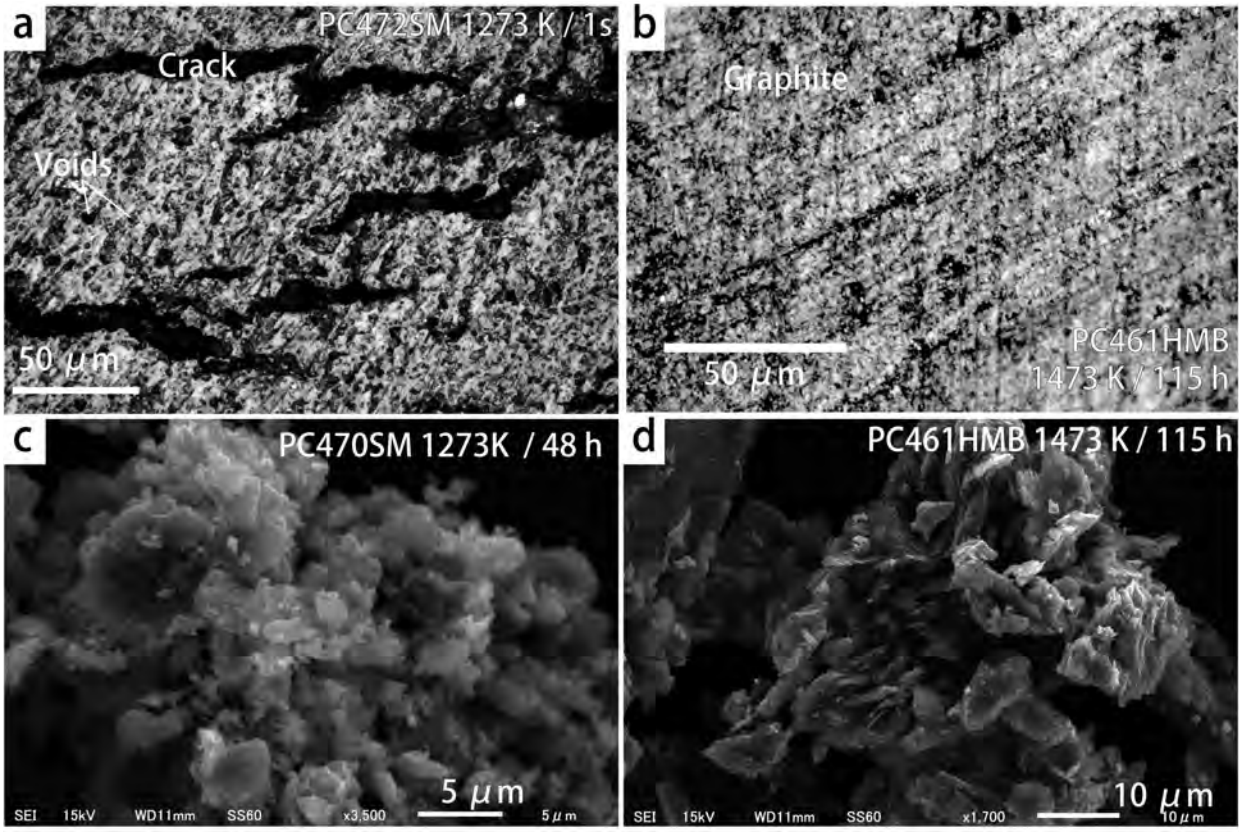

Figure 1. Optical and backscattered images of the run products extracted from various time–temperature experiments. (**a**) Photomicrograph of a polished slab section of sample PC 472SM showing many voids and cracks (1000 °C, 1 GPa, 1 s). (**b**) Photomicrograph of the smooth surface of sample PC 461HMB (1200 °C, 1 GPa, 115 h). (**c**) Porous structure of powder CM extracted from the Pt capsule for sample PC470SM (1000 °C, 1 GPa, 48 h). (**d**) Planar structure of powder CM extracted from the Pt capsule for sample PC461HMB (1200 °C, 1 GPa, 115 h).

(1000–1800 cm^{-1}; Fig. 2b; Appendix[1] Table 1). Their intensity and area ratio gradually change with increasing temperature and longer treatment. In addition to the first-order region, the overtone and combinations of the G and D bands (2D1, D1+G, 2D2) in the second-order region (2500–3200 cm^{-1}) show similar changes to the main bands, as reported by Wopenka and Pasteris (1993). At the early stage of annealing at low temperature, disordered bands such as D3 and D4 are identified by the peak deconvolution of two prominent bands (Fig. 2b). The 1500 cm^{-1} D3 band generally appears broad, suggesting that it originates from amorphous sp^2-bonded carbon from organic molecules, fragments, or functional groups in poorly organized materials (Cuesta et al. 1994; Sadezky et al. 2005). The 1200 cm^{-1} D4 band is also derived from poorly organized organic materials, and is attributed to sp^3–sp^2 mixed sites at the peripheries of crystallites or to C–C and C=C stretching vibrations of polyene-like structures (Dippel and Heintzenberg 1999; Sadezky et al. 2005; Sheng 2007). These two bands indicate that the CM samples at the early stage of annealing at low temperatures have many dangling bonds on polyaromatic layers. Higher temperatures and longer annealing change the CM into a graphitic structure, as shown by the decreasing intensity of the disordered bands. These structural changes observed by micro-Raman spectroscopy are in a good agreement with those observed by XRD. Beyssac et al. (2003) reported that the crystal parameters in micro-Raman spectroscopy display strong heterogeneous distributions in microscopic scale. To assess the microtextural heterogeneity, we compared the area ratio of the center with the edge part of non-polished slab section of platinum capsules (Fig. 3). The edges of both samples annealed at lower temperatures show slightly lower crystallinity compared with the central part of the capsule. This may have resulted from the temperature and microstructural heterogeneity within the assembly as reported by Beyssac et al. (2003). However, almost all data obtained in the temperature range exhibited a strong squared correlation coefficient of 0.978 in the center vs. the edge parts of area ratio plot (Fig. 3).

TEM observations

The starting materials of HMB and SM show different microstructural signatures. Although the CMs of HMB display broad 002, 10, and 11 rings in the selected-area electron diffraction (SAED) patterns, poorly crystallized parallel fringes are locally observed in the tissue-like aggregates (Fig. 4a). Under high magnification, poorly organized fringes surrounded by disordered graphitic layers are discernible. The distorted graphitic layers

[1]Deposit item AM-16-15733, Supplemental Table. Deposit items are free to all readers and found on the MSA web site, via the specific issue's Table of Contents (go to http://www.minsocam.org/msa/ammin/toc/2017/Jan2017_data/Jan2017_data.html).

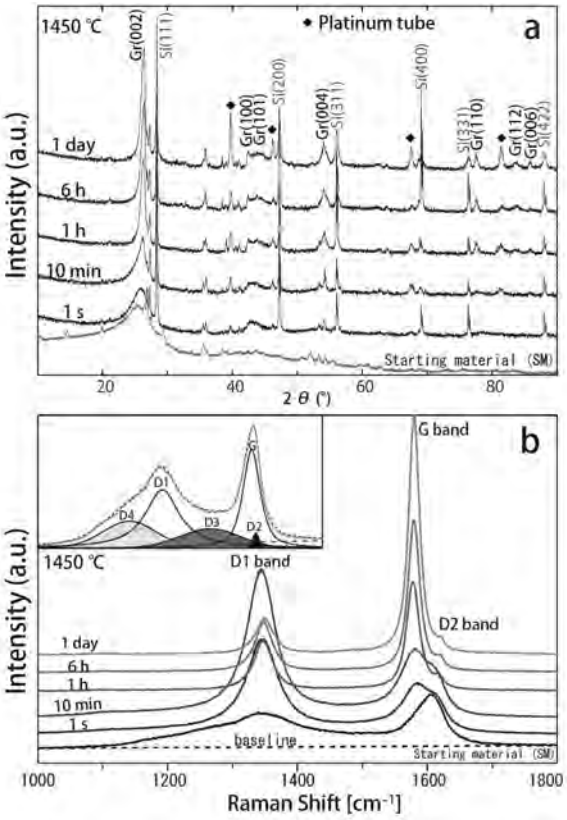

FIGURE 2. Structural evolutions from 1s to 24 h of CM and starting material in SM to graphite at 1450 °C as observed by (**a**) X-ray diffractometry and (**b**) micro-Raman spectroscopy. The Raman spectra of CM are fitted by five peaks of D1, D2, D3, D4, and G band. Silicon peaks in XRD profile are an internal standard for calibrating the interlayer spacing of disordered graphite.

TABLE 2. Experimental conditions and XRD profiles of the run products at 1 GPa

Run no.	T (°C)	t (min)	XRD analysis							
			CM in Hidaka metamorphic belt				CM in Shimanto accretionary complex			
			d_{002} (Å)	FWHM	L_c(002) (Å)	g^* (%)	d_{002} (Å)	FWHM	L_c(002) (Å)	g^* (%)
PC478	1000	10	3.432	2.58	35	0.019	3.491	5.33	17	0.035
PC475	1000	60	3.426	2.39	38	0.099	3.495	4.67	19	0.008
PC473	1000	360	3.420	2.39	38	0.170	3.483	4.75	20	0.093
PC471	1000	1440	3.406	2.19	41	0.356	3.471	3.59	25	0.186
PC470	1000	2880	3.402	2.12	43	0.416	3.471	3.48	26	0.184
PC482	1200	0.017	3.430	2.45	37	0.044	3.436	4.04	22	0.439
PC477	1200	10	3.427	1.93	47	0.083	3.430	2.91	31	0.483
PC479	1200	30	3.417	1.93	47	0.212	3.437	2.43	37	0.436
PC476	1200	60	3.416	1.66	55	0.226	3.420	2.55	36	0.556
PC485	1200	180	3.396	1.19	69	0.492	3.396	1.38	65	0.739
PC474	1200	360	3.393	1.14	80	0.538	3.396	1.51	60	0.738
PC462	1200	1440	3.387	0.89	107	0.619	3.382	0.72	127	0.840
PC461	1200	6900	3.359	0.40	225	0.989	3.368	0.70	129	0.941
A2590	1325	10	3.404	1.40	65	0.390	3.422	2.31	39	0.543
A2588	1325	60	3.387	1.20	76	0.607	3.400	0.76	119	0.708
A2583	1325	360	3.369	0.80	113	0.853	3.372	0.62	147	0.915
A2581	1325	720	3.362	0.61	146	0.947	3.368	0.64	154	0.938
A2582	1325	1440	3.368	0.63	144	0.868	3.370	0.59	143	0.926
A2580	1325	2880	3.367	0.45	201	0.875	3.368	0.60	152	0.938
PC481	1450	0.017	3.407	1.47	62	0.351	3.425	1.17	37	0.523
A2589	1450	10	3.388	1.25	72	0.607	3.383	0.57	77	0.831
A2587	1450	60	3.365	0.79	115	0.903	3.375	0.55	159	0.891
A2586	1450	360	3.364	0.67	136	0.927	3.373	0.51	179	0.906
A2584	1450	1440	3.367	0.40	228	0.881	3.363	0.49	184	0.975

Note: L_c(002) is calculated by the Scherrer equation (K = 1.0). g^* (%) is the calculated degree of crystallinity using initial and final values of d_{002} spacing.

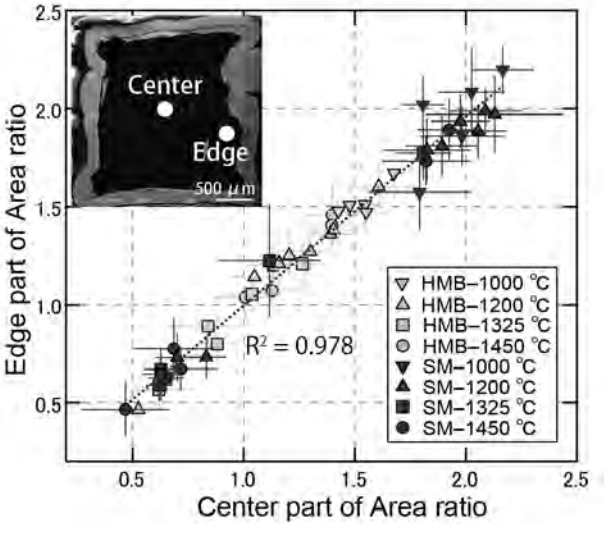

FIGURE 3. Relationship between center and edge parts of area ratio (D1+D4 bands)/(D2+D3+G bands). The dashed line is calculated by linear regression.

already have anisotropy in lateral direction. The SAED pattern in the distorted graphitic layers shows arc-like spots of 002 reflections, suggesting turbostratic structures within graphitic layers (Fig. 4b). Such aggregates of CM were also observed in the chlorite zone (Buseck and Huang 1985). On the other hand, the CMs of SM also show broad 002 rings in the SAED patterns and granular aggregates (Fig. 4c). Under high magnification, poorly organized fringes that are composed of 2–3 carbon layers are observed. In contrast to the CM in HMB, the poorly organized fringes are isotropically oriented in the aggregates (Fig. 4d). The isotropic distributions of poorly organized fringes generally correspond to the nanostructure of BSU in coal (Oberlin et al. 1999). Longer and higher-temperature annealing converts these nanostructures to a graphitic structure (Figs. 4e–4h). Under the 11 dark-field (DF) mode, the platy graphite displays a typical moiré fringe, suggesting a fully ordered and stiff layer in lateral direction (Fig. 4e; Oberlin 1984). In addition, the 10 ring in the SAED pattern starts to split into two diffraction patterns of 100 and 101 spots, while the 11 ring splits into 110 and 112 spots (Fig. 4g). The lattice fringes of the d_{002} spacing are fully ordered, and define (002) and (101) in the SAED pattern along the [010] direction (Figs. 4f and 4h). These microstructural observations suggest that heat treatment converted both CM samples to a graphitic structure. However, the SAED patterns still display ring and spotted patterns, suggesting the presence of turbostratic or amorphous structures in the graphitic carbon. In fact, some of the XRD peak profiles show asymmetric d_{002} peaks, which included signatures of both the turbostratic and graphitic components in the microstructure. Previous studies using XRD (Inagaki and Meyer 1999), micro-Raman spectroscopy, and TEM observations (Beyssac et al. 2003) have reported that graphitization under

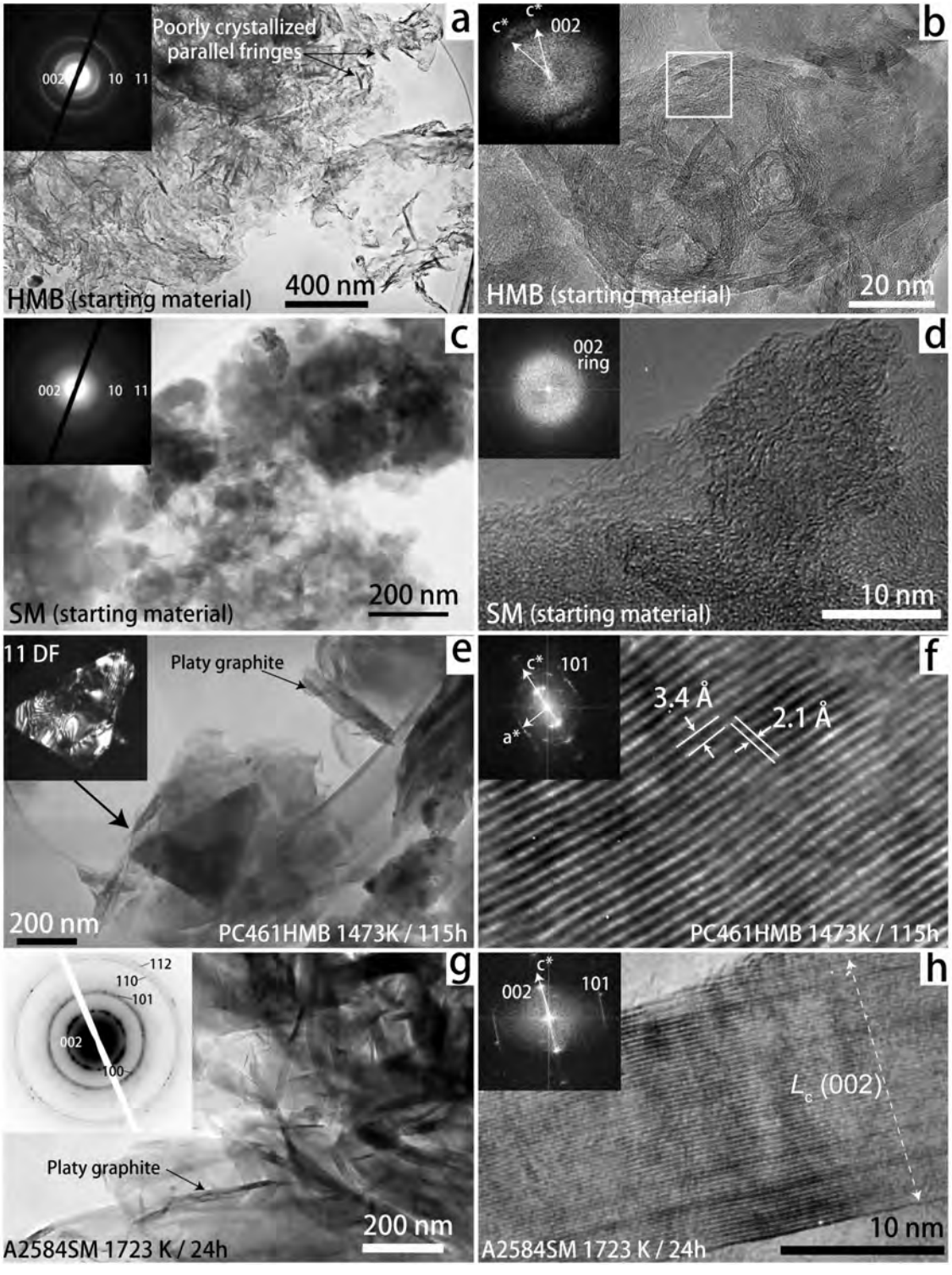

Figure 4. Microstructural evolutions of the CM in HMB and SM to graphite. (**a**) TEM image and corresponding SAED pattern of the starting material in HMB. The distorted graphitic layers are locally observed in the tissue-like aggregates. (**b**) High-magnification image of the poorly crystalline carbon surrounded by the distorted graphitic layers. The SAED pattern is compiled from the area outlined by the white square. (**c**) TEM image and corresponding SAED pattern of the starting material in SM. (**d**) High-magnification image and SAED pattern of poorly organized fringes. (**e**) TEM image of ordered graphite and its 11 dark-field image (PC461HMB, 1200 °C and 115 h). (**f**) Lattice fringes of graphite corresponding to (002) and (101) along the [010] direction. (**g**) Nanostructures and corresponding SAED pattern of ordered graphite (A2584SM, 1450 °C and 24 h). (**h**) Lattice fringes and corresponding SAED pattern of ordered graphite.

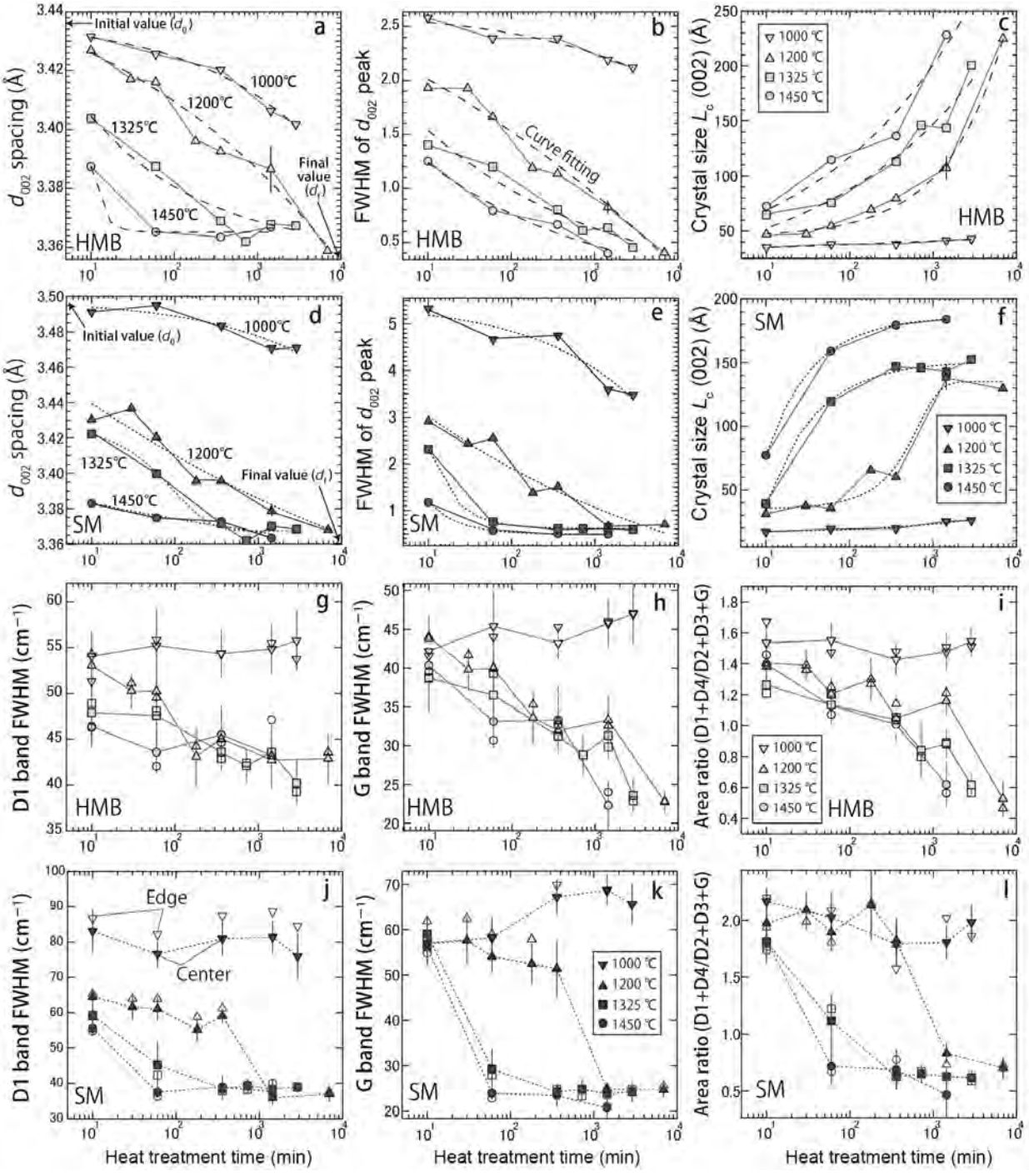

FIGURE 5. Time–temperature relations between 10 and 10^4 min. The parameters (**a**) d_{002} spacing, (**b**) FWHM of d_{002} peak, and (**c**) L_c(002) from XRD, and also (**g**) D1 band FWHM, (**h**) G band FWHM, and (**i**) area ratio are based on data for the CM in HMB. (**d**, **e**, **f**, **j**, **k**, and **l**) show the same parameters, respectively, for the CM in SM. Data from XRD are used to calculate the non-linear best fitting of sigmoid functions and power functions for reference.

HPHT conditions induces heterogeneous recrystallization. In this study, similar patterns regarding microstructural evolution observed by TEM supports their results observed in XRD and micro-Raman spectra.

Time–temperature relations inferred from heat treatment

The time–temperature relations of both CM samples display changes in crystallinity with increasing annealing duration (Figs. 5a–5l). Similar to the observations of Beyssac et al. (2003),

structural changes at 1000 °C were limited when annealing lasted between 10 min and 48 h. However, structural changes of CM to graphite occurred at 1200, 1325, and 1450 °C as the heat treatment progressed. In particular, almost all the crystal parameters indicated a graphitic structure even at the early stage of heating (1–6 h), and most of the parameters became constant or showed only extremely slow change after 6 h, suggesting either the termination of crystal growth or only sluggish growth. In addition, each parameter obtained from XRD and micro-Raman spectroscopy displays some important signatures in the time–temperature relations. The d_{002} spacing (Figs. 5a and 5d) and FWHM (Figs. 5b and 5e) for both CM samples terminate at around 3.36 Å and 0.4°, respectively. The $L_c(002)$ of SM (Fig. 5f) also indicates the termination of crystal growth at around 200 Å, whereas that of HMB (Fig. 5c) still grow up over 200 Å in crystal thickness. The unchanging d_{002} spacing indicates the formation of graphitic structures in the microstructures, but the termination of crystal growth shows a different signature from both samples. In general, the final crystal sizes of carbon materials such as carbon black and soft carbon directly depends on the primary nanostructures (spherical or platy) during graphitization (Inagaki 1996). The starting material of SM displayed isotropic poorly organized fringes (Fig. 4d), whereas that of HMB already had developed the anisotropic distorted layers (Figs. 4a and 4b). The different primary nanostructures considered here may have influenced the final crystal sizes and morphological characteristics of the run products.

Discussion

Kinetic models of graphitization

The results of the HPHT experiments at 1 GPa for both CM samples suggest that their changes in crystallinity, morphology, and nanostructures were directly related to both the duration and temperature of treatment. We therefore assessed three different kinetic approaches of graphitization using the power rate model (e.g., Murty et al. 1969), the Johnson-Mehl-Avrami (JMA) model (e.g., Sung 2000; Khawam and Flanagan 2006) and the superposition method (e.g., Fischbach 1963; Inagaki et al. 1968). Before we adopted these kinetic models, the experimental data were converted to the degree of graphitization (g) by following the equation (Murty et al. 1969; Khawam and Flanagan 2006; Table 2):

$$g = (d_0 - d_1)/(d_0 - d_f) \quad (1)$$

where d_0 is the initial value of d_{002} spacing (Figs. 5a and 5d; Fischbach 1971), d_1 is the observed experimental data, and the d_f show the final value of d_{002} spacing (Figs. 5a and 5d; Fischbach 1971). The power rate model is the most robust kinetic model for carbonization and widely applied for extrapolating the geological time–temperature regime using the rate constant and pre-exponential factor (e.g., Huang 1996). After conversions to nondimensional parameters, we attempted to fit the following power law of time as:

$$g = k_p t^{-n} \quad (2)$$

where k_p is the rate constant, t time (s), n an order of reaction at that temperature. The experimental data fitted by the Equation 2 show squared correlation coefficient of 0.584–0.952 depending on the treatment temperatures (Figs. 6a–6b). The rate constant k_p and order of reaction n also demonstrate distributions as a function of the treatment temperature. In particular, the logarithm of rate constant $\ln k_p$ and order of reaction n show strong squared correlation coefficient of 0.979 (Fig. 7). This suggests that the kinetics of graphitization under low and high temperature underwent different chemical reactions. Some previous studies have used the mean values of order of reaction (Huang 1996) or linear regression values from the least squares of experimental data (Muirhead et al. 2012) to avoid the experimental uncertainty of the complex chemical reactions. The differences of experimental uncertainty are permissible in the range of order of reaction (n) between 0.062 and 0.09 (Huang 1996). On the other hand, the orders of reaction in this study vary widely (n = 0.007 to 0.82), and it is difficult to apply the previous methods directly (Fig. 7). The results imply that graphitization is not a simple chemical reaction and that various reactions progress simultaneously (parallel reaction) and/or successively (successive reaction). In this study, we attempted to fit the Arrhenius relation using following equation:

$$k_p = A\exp(-E_a/RT) \quad (3)$$

where k_p is the rate constant, A the pre-exponential factor, E_a the effective activation energy, R the gas constant, and T the absolute temperature of the experiment. Using the Arrhenius Equation 3, we calculated the effective activation energy. The values of SM and HMB samples partly demonstrate good squared correlation coefficients of 0.903 and 0.981, however, have a large uncertainty spread in the average of activation energies of 259 ± 26 and 271 ± 63 kJ/mol (Fig. 6c; Table 3). Consistent with the results of earlier experimental studies, we concluded that graphitization does not follow a simple power rate model (e.g., Fischbach 1971).

Instead of a power rate model, we tried to calculate the best fitting using a JMA model to apply for the complex "sigmoid" transformation from an amorphous to a graphitic structure (Figs. 5a–5l). The JMA equation is suitable to heterogeneous nucleation and recrystallization and widely applied in material science (e.g., Khawam and Flanagan 2006). The equation was expressed as follows:

$$g = 1 - \exp(-k_a t^l) \quad (4)$$

where k_a is the rate constant of JMA equation, l is the order of reaction named for "Avrami index," t is the duration of heating (s). Taking the natural logarithm of Equation 4, it can be also expressed as:

$$\ln[-\ln(1 - g)] = \ln k_a + l\ln t. \quad (5)$$

Plotting the left side of equation ($\ln[-\ln(1 - g)]$) and natural logarithm of time $\ln t$, the rate constant k_a and Avrami index l are estimated from the linear regression of intercept and slope in this Avrami plot, respectively. The model fitting by a JMA equation displays squared correlation coefficient between 0.555 and 0.963 depending on the temperatures (Figs. 6d–6e). The rate constant k_a and order of reaction l also demonstrate distributions as a function of the temperature (Fig. 7). Such variations are consistent with the results of the power rate model, suggesting complex chemical reactions. Using the $\ln k_a$ values vs. $1/T$, we obtained the effective activation energies of 269 ± 59 and 273 ± 47 kJ/mol for HMB and SM samples, respectively (Fig. 6f; Table 3). Both models are not in good agreement with the experimental

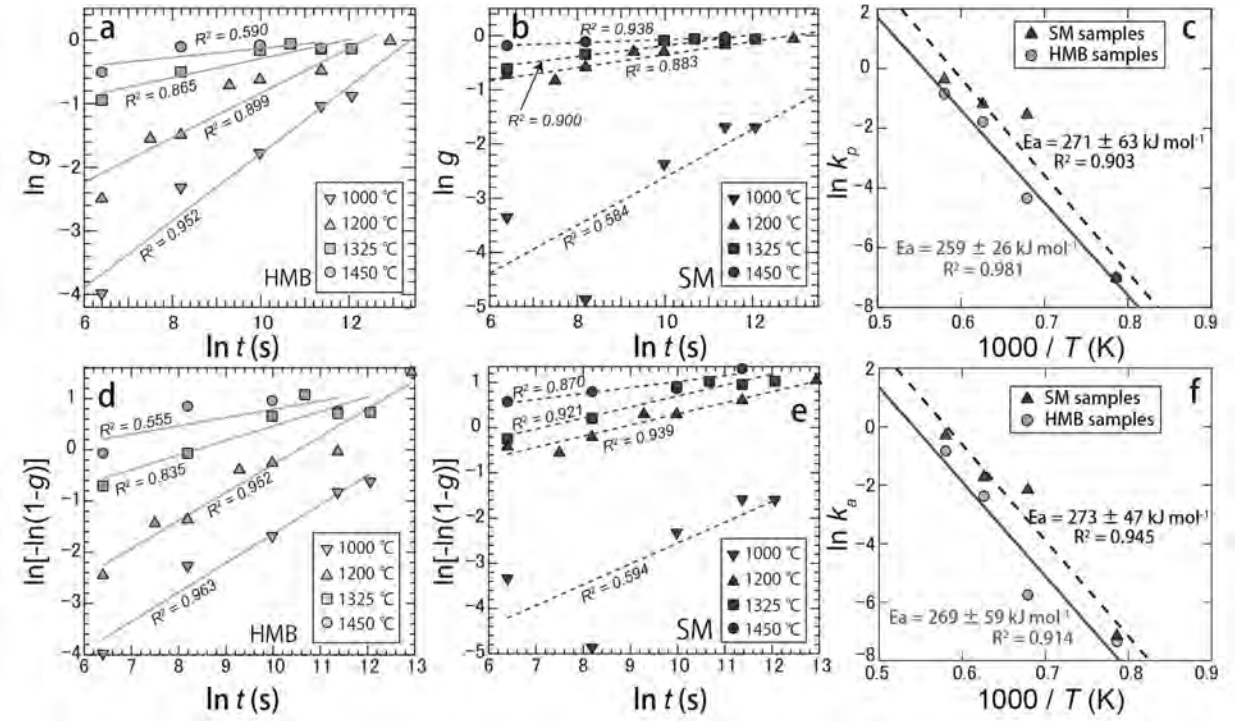

Figure 6. The relationship between experimental ln*t* (s) and ln*g* of HMB (**a**) and SM samples (**b**) fitted by a power rate model. (**c**) Arrhenius plot of HMB and SM samples. The relationship between experimental ln*t* and ln[–ln(1–*g*)] of HMB (**d**) and SM samples (**e**) fitted by a JMA model. (**f**) Arrhenius plot of HMB and SM samples.

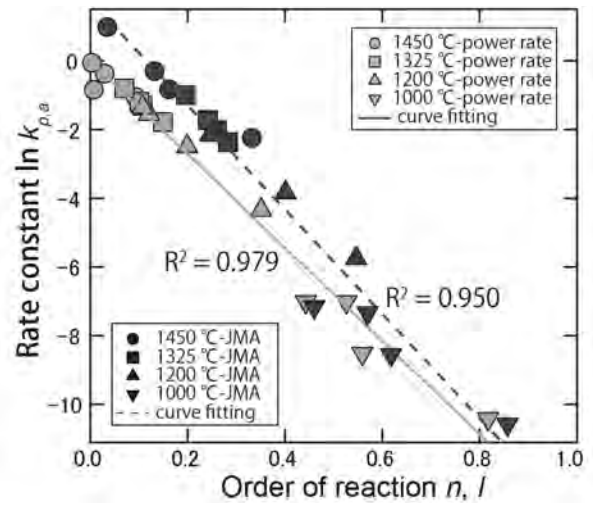

Figure 7. The relationship between the rate constants ln$k_{p,a}$, and the orders of reaction *n*, *l* of power rate, and JMA models. All of rate constants and orders of reaction including d_{002} spacing, FWHM of d_{002} peak, L_c(002), and area ratio and are plotted.

structural changes from CM to graphite. These misfits to model fitting result from the large variation of the effective activation energies. Thus, we concluded that the structural change of CM to graphite cannot follow a simple power rate model nor a simple JMA model.

We therefore applied the superposition method to propose a kinetic model for natural graphitization. The effective activation energy is usually obtained from the slope of the Arrhenius plot, which is the logarithm of the rate constant vs. the reciprocal of absolute temperature (i.e., ln*k* vs. 1/*T*). Arrhenius plots using a power rate model and a JMA model empirically provide only one intercept value (ln*k*) for each treatment temperature, whereas the superposition method has an advantage in its determination of the activation energy using two or more slopes derived from all experimental data. This is an effective method to predict the kinetics of complex chemical reactions. The superposition method is well known to describe the mechanical and electrical relaxation behavior of polymers, and some earlier studies have successfully applied the Arrhenius approach to graphitization (e.g., Fischbach 1971; Feng et al. 2002). The fitting curves of the measured crystal parameters vs. the logarithmic treatment time at different temperatures can be superposed by proper

Table 3. Summary of rate paramters calculated from power rate and JMA models

Crystal parameter	Kinetic model	*m*	ln*A* (s)	E_a (kJ/mol)	R^2
d_{002} spacing-HMB	power rate	–31103 (3070)	17.27 (2.06)	259 (26)	0.981
d_{002} spacing-SM	power rate	–32569 (7560)	19.21 (5.08)	271 (63)	0.903
d_{002} spacing-HMB	JMA	–32414 (7040)	17.50 (4.73)	269 (59)	0.914
d_{002} spacing-SM	JMA	–32886 (5620)	19.12 (3.78)	273 (47)	0.945

scale changes on the time axis. The shift in distance is called the time–temperature shift factor a_T, which is given by:

$$a_T = t_T/t_{ref} \quad (6)$$

where t_{ref} is the reference time at a certain reference temperature (Fig. 8a), and t_T is the time required to give the same response at the reference temperature (Fig. 8a). For every reference temperature chosen, a fully superimposed curve generated by the shift factors is called the master curve. The above Equation 6 also can be written by combining the Arrhenius Equation 3:

$$a_T = \exp\{E_a/R\ (1/T - 1/T_{ref})\} \quad (7)$$

where both T and T_{ref} are absolute temperatures. Plotting $\ln(a_T)$ vs. $1/T$ is another way to calculate E_a values and to predict crystal changes at low temperatures. The crystal properties with regression curves obtained by the superposition method are shown in Figure 8 and Table 4. The experimental reference temperature here is 1000 °C. To find the best-fitting non-linear regression curve, some sigmoid functions and power functions were chosen to determine the shift values (Table 4). The fitting considered four parameters: the unit-cell height c, the FWHM of the d_{002} peak, $L_c(002)$, and the area ratio of the Raman bands. The master curves obtained for both samples show good squared correlation coefficients of 0.878 to 0.982 (Figs. 8a–8d; Table 4). In particular, these sigmoid functions accurately reflect the three different processes of the successive reactions from carbonization to graphitization. The first stage of heat treatment corresponds to the formation of BSUs by the release of aliphatic and aromatic C–H bonding. After devolatilization, they start to crystallize from turbostratic to graphitic structures as the temperature and duration increase. The final transformation to graphite suggests the termination of crystal growth. Our extrapolations using sigmoid fitting have an advantage over the linear or power law fitting models used in previous studies, because we can extrapolate from the starting point to the termination point using a single sigmoid master curve. The effective activation energy was calculated from the relationship between $\ln(a_T)$ and $1/T$. The plot of the mean values and their linear regression lines show good squared correlation coefficients of 0.984–0.999 (Table 4), suggesting that the relation between annealing duration and temperature can be described as a thermal activation process. The mean values

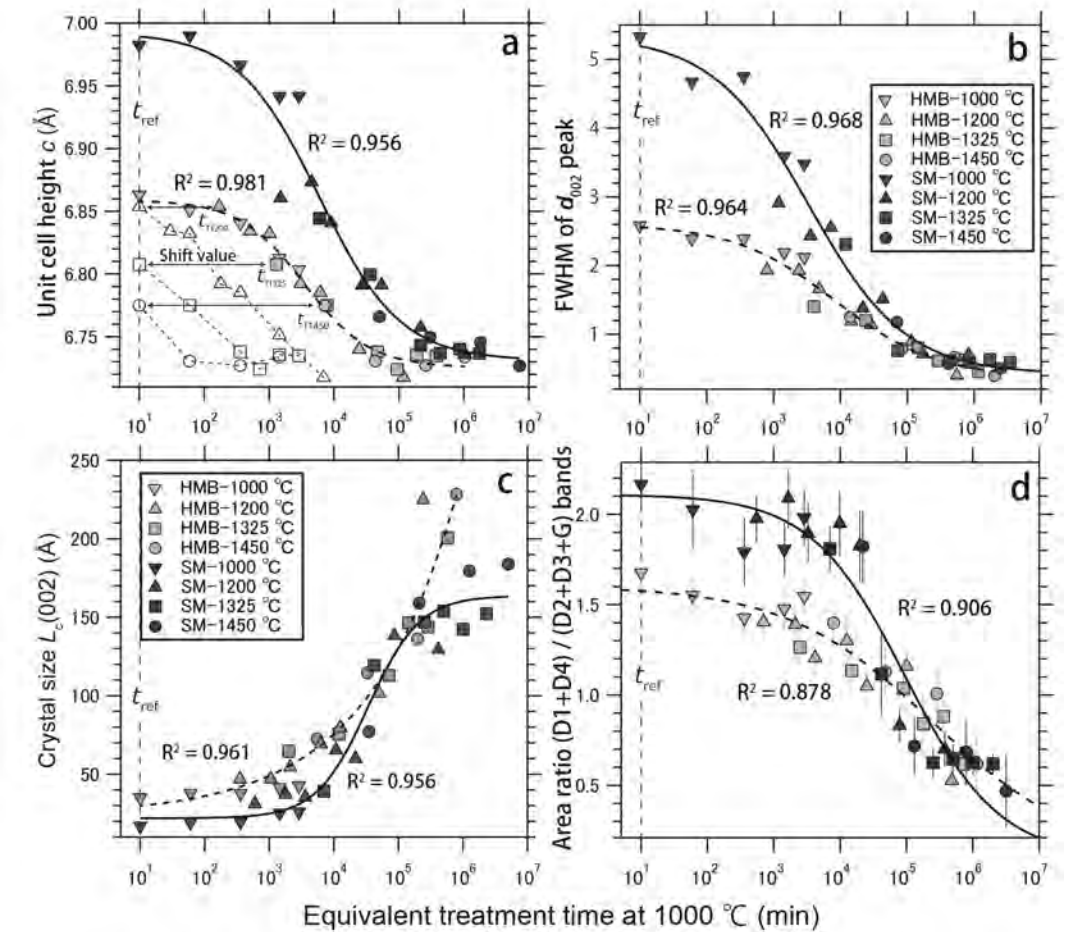

FIGURE 8. Composite master curves for CM samples SM and HMB obtained by shifting the 1200, 1325, and 1450 °C curves to combine smoothly with the 1000 °C (reference temperature) curve from time–temperature relations. All master curves are calculated by non-linear best fitting of sigmoid functions and power functions. Master curves of both CM samples are fitted by the values of (**a**) unit-cell height c, (**b**) FWHM of d_{002} peak, (**c**) $L_c(002)$, and (**d**) area ratio.

TABLE 4. Summary of calculated E_a values and fitting results

Parameters	Samples	Fitting data (sigmoid function) C_{min}	C_{max}	h	t_{half}	R^2	Arrhenius plots m	ln$A$	lnA_1[a]	E_a (kJ/mol)	R^2
d_{002} spacing	HMB	6.859 (6)	6.725 (4)	0.86 (12)	3577	0.982	−31893 (2230)	24.86	−16.680	265 (19)	0.990
FWHM	HMB	2.60 (14)	0.36 (14)	0.57 (12)	8482	0.964	−35641 (2380)	28.20	−19.154	296 (20)	0.990
Area ratio	HMB	1.60 (10)	0.10	0.39 (8)	247240	0.878	−32776 (2930)	26.00	−13.563	272 (24)	0.984
d_{002} spacing	SM	6.992 (17)	6.731 (11)	0.69 (14)	5905	0.957	−40813 (2750)	32.23	−23.546	339 (23)	0.991
FWHM	SM	5.34 (32)	0.42 (16)	0.60 (11)	3358	0.969	−43416 (860)	34.17	−26.050	361(7)	0.999
L_c(002)	SM	21.98 (6.4)	163.70 (7.4)	1.09 (26)	33813	0.956	−40198 (1090)	31.54	−21.104	334 (9)	0.999
Area ratio	SM	2.11 (11)	0.10	0.61 (10)	95374	0.906	−38508 (2110)	30.27	−18.808	320 (18)	0.994
		Fitting data (Power function[b]) c	A	b	R^2						
L_c(002)	HMB	23.9 (13.6)	2.9	0.31 (6)	0.961		−31312 (1520)	24.70		260 (13)	0.995

[a] lnA_1 is calculated from the intercept of the Arrhenius plot ($1/T$ vs. lnt_{half}). [b] $f(t) = A\exp(bt) + c$.

of effective activation energies were 274 ± 9 and 339 ± 6 kJ/mol for HMB and SM, respectively (Fig. 9).

The estimated activation energies between 259 and 339 kJ/mol using a power rate model, a JMA model and a superposition method are remarkably lower than the previously determined activation energies (~1000 kJ/mol) under 1 atm. Summarizing the previous studies and our results, we found that the effective activation energies systematically decrease as a function of pressure (Fig. 10). Some previous studies pointed out that the structural evolution of CM to graphite rapidly progress by additional pressure (Beyssac et al. 2003; Zhao et al. 2009). However, these studies only noted the possibility of fast graphitization under high pressure and detailed investigation of kinetics under high pressure is limited. Noda et al. (1968) argued that graphitization under high pressure changes the E_a values from 1000 to 330–500 kJ/mol by additional pressure of 0.3–0.5 GPa. Such a large pressure dependence on graphitization was also observed in this study. According to the results of Lynch and Drickamer (1966) and Hanfland et al. (1989), the crystal thickness (L_c) and diameter (L_a) in a graphitic structure decrease by about 2.2 and 0.17% at 1 GPa at room temperature, respectively. The interlayer spacing of graphite decreases by about 2.5% with development of the graphitic structure. Thus, the decrease at 1 GPa is comparable to the total decrease of interlayer spacing during graphitization. Such a large effect on compression along the *c*-axis may result from a "negative" activation volume under HPHT experiments. In the light of pressure dependence, the activation energy under high pressure is strictly expressed by the equation: $\Delta H = \Delta E_a + P\Delta V^{\neq}$, where ΔH is the activation enthalpy, ΔE_a the activation energy at 1 atm, P the pressure, $\Delta V^{\neq}$ the activation volume. If the ΔH values are correlatable to a single effect on pressure dependence, the ΔH values and pressure P will show a linear relationship, and the ΔE_a and $\Delta V^{\neq}$ values can be calculated from the intercept and slope, respectively. In this study, the relation between the effective activation energy and pressure seems to display a logarithmic curve rather than a linear regression line (Fig. 10). This may suggest that the different factors are included in the whole "effective" activation energies. For instance, Marsh et al. (1983) reported that catalytic effects largely change the activation energy from 1000 to ~400 kJ/mol without addition of pressure. Although it is uncertain to calculate the activation volume using our results, we found that the activation energies between ambient pressure and 1 GPa decrease by a factor of over 2. Thus, almost all natural graphitization in the Earth's crust undergoes a faster transformation than estimated in previous studies.

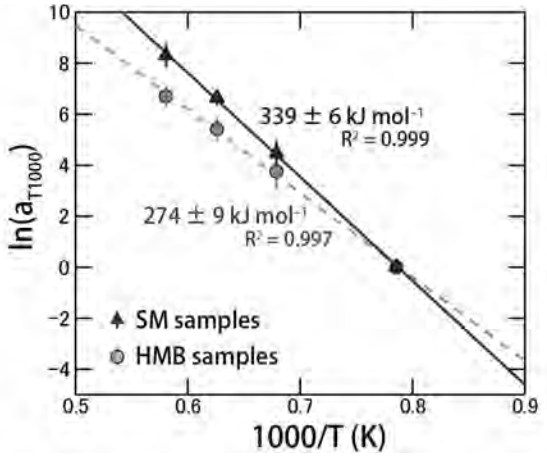

FIGURE 9. Arrhenius plot of shift values using the average of four different parameters by XRD and micro-Raman spectroscopy. Error bars show one standard deviation.

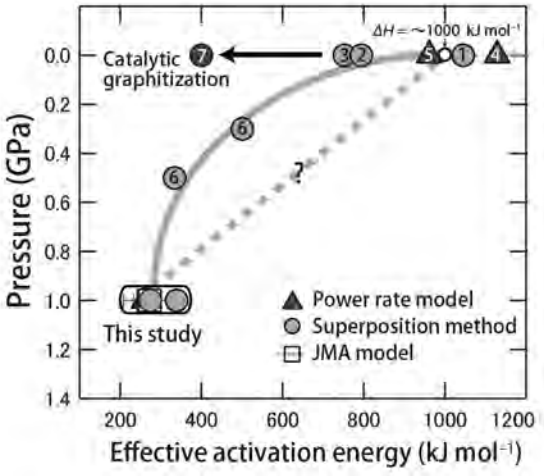

FIGURE 10. Compilation of effective activation energies (kJ/mol) at various pressures (GPa) obtained in this study and published values using power rate model, JMA model, and superposition method. The effective activation energies of previous studies are cited from 1 = Fischbach (1963); 2 = Inagaki et al. (1968); 3 = Noda et al. (1965); 4 = Fischbach (1971); 5 = Murty et al. (1969); 6 = Noda et al. (1968); and 7 = Marsh et al. (1983).

IMPLICATIONS

Our experimental kinetic study on the structural evolution of CM to graphite gave remarkably low activation energies for the natural precursor materials, and natural graphitization in the Earth's crust may proceed much more quickly than suggested by previous calculations based on large activation energies (~1000 kJ/mol) because of "negative" activation volume during graphitization. This suggests that extrapolation using our kinetic model at 1 GPa is expected to model well the conditions of geological environments and produce better results than previous studies. Based on the experimental results in this study, we attempted a simplified isothermal calculation of graphitization rate depending on temperature. If graphitization rate is subject to Arrhenian temperature dependence, the sigmoid master curves can be extrapolated to represent low-temperature conditions. For instance, sigmoid fitting was tested using the parameters of unit-cell height c, and the area ratio (AR) of Raman spectra:

$$f(t) = C_{min} + (C_{max} - C_{min})/\{1 + (t_{half}/t)^h\} \quad (8)$$

where C_{min} and C_{max} are, respectively, the maximum and minimum values of each parameter, t is the annealing duration during metamorphism, t_{half} is the inflection point obtained from this function, and h is the order of reaction of the sigmoid function (called "Hill coefficient"). The values of C_{min} and C_{max} correspond to the starting and termination points of natural graphitization, respectively, and h is used for the experimental data (Table 4). The value of t_{half} changes as functions of time and temperature. Therefore, we calculate its value at target temperature and time from the Arrhenius plots. The t_{half} can also be described following the Arrhenius relation:

$$t_{half} = A_1 \exp(-m/T) \quad (9)$$

where A_1 is the intercept and m is the slope of the Arrhenius plot. Combining Equations 8 and 9:

$$f(T, t) = C_{min} + (C_{max} - C_{min})/[1 + \{A_1 \exp(-m/T)/t\}^h]. \quad (10)$$

It is thus possible to predict the structural evolution of CM to graphite by the above function of peak temperature T (K) and annealing duration t (min) during metamorphism. Using the above Equation 10, we attempted to extrapolate the structural evolution of CM to graphite at low temperatures (300–800 °C) during annealing for 1–10^{10} years. For instance, the master curve at 1000 °C extended to ~10^6 min (~2 years) for the formation of graphite (Figs. 8a–8d). With decreasing temperature, the time required for conversion to graphite exponentially increases. Figure 11 shows the calculated time–temperature transformation diagrams using the parameters of unit-cell height c (Figs. 11a and 11c) and the area ratio (AR) of Raman spectra (Figs. 11b and 11d). If CM in HMB underwent prograde metamorphism for about 10000 years, it would show initial crystallinity changes at ~500 °C and conversion to the fully ordered graphite (d_{002} spacing ~3.36 Å) at over ~640 °C (Path 1 of Fig. 11a). Longer metamorphism for ~1 m.y. would convert CM to fully ordered graphite at temperatures over ~520 °C (Path 2 of Fig. 11a). The CM in SM shows a similar change in its crystallinity as a function of duration (Paths 5 and 6 of Fig. 11c), however, the estimated temperatures at the conversion of graphite are slightly higher than that in HMB. This difference results from the difference in the initial activation energy required to form a graphite. Wang (1989) reported that almost fully ordered graphite (d_{002} spacing ~3.36 Å) in high-pressure low-temperature and high-temperature low-pressure metamorphic rocks can form at temperatures between 410 and 440 °C in various metamorphic terrains. Our kinetic model suggests that annealing following metamorphism requires ~10^8 years (Fig. 11a). The results are not in good agreement with natural and calculated graphitization rates. In addition to unit-cell height c, the area ratio (AR) in HMB and SM also displays similar behavior as a function of heating duration (Figs. 11b and 11d). If CM in HMB underwent prograde metamorphism for about 10000 years, it would show initial crystallinity changes at 350 °C and conversion to graphite (AR < 0.2) at over 800 °C (Path 3 of Fig. 11b). Longer metamorphism for ~1 m.y. would convert CM to graphite at temperatures over ~20 °C (Path 4 of Fig. 11b). The CM in SM displays initial crystallinity changes at 350 °C and conversion to graphite at over 590 °C for duration of ~1 m.y. (Path 8 of Fig. 11d). In contrast to the unit-cell height c, the contour of AR tends to extend over a wide interval in time-temperature space (Figs. 11b and 11d). The difference is driven by the calculated Hill coefficient h in Equation 10, making AR a more sensitive measure for graphitization progress over a wide temperature range. In the case of micro-Raman spectroscopic studies, almost all CM changed into graphite at around 650 °C based on the detailed observations of various types of metamorphic terrains (Beyssac et al. 2002; Aoya et al. 2010; Hilchie and Jamieson 2014). If CMs changed into graphite at 650 °C by graphitization, the durations of heating required would be about 100000 years (SM) and 10 m.y. (HMB), respectively. These estimations suggest that natural CMs are rapidly able to change their crystallinity as functions of realistic duration and peak temperature. In particular, the structural change of CMs in SM are consistent with previously reported examples of natural graphitization (Beyssac et al. 2002; Aoya et al. 2010), where crystallinity increased at temperature between 350 and 650 °C. This suggests that the Raman spectra of carbonaceous materials (RSCM) thermometry have potential to be calibrated to use the Arrhenius-type t-T dependence of graphitization as a tool for extracting kinetic information from natural rocks. On the other hand, we found that the two CM samples display a large divergence of recrystallization. This difference results from the sigmoid t-T-relation descried by the Hill coefficient h, and suggests that further detailed evaluation of the chemical reaction under natural and laboratory conditions are required for a complete understanding of structural evolution of CM.

Overall, our kinetic model demonstrates that graphitization can proceed at relatively low temperatures (520~720 °C) in generally more realistic timescales (~1 m.y.) than expected from previous experimental kinetic studies (e.g., Fischbach 1971). In addition, our new kinetic data suggests that activation energies as reported previously (e.g., Fischbach 1971) do not suitably describe natural graphitization in crustal settings. Under a lithostatic pressure of 1 GPa, we were able to demonstrate the structural evolution of CM at geologically reasonable temperatures (300–800 °C) and durations (1–10^{10} years). Further refining and a better understanding of the kinetics of graphitization might provide new pathway to use it not only as a tool for geothermometry but also for geospeedometry to resolve petrogenetic processes occurring over geologic timescales. However, there exist slight mismatch between our experimental

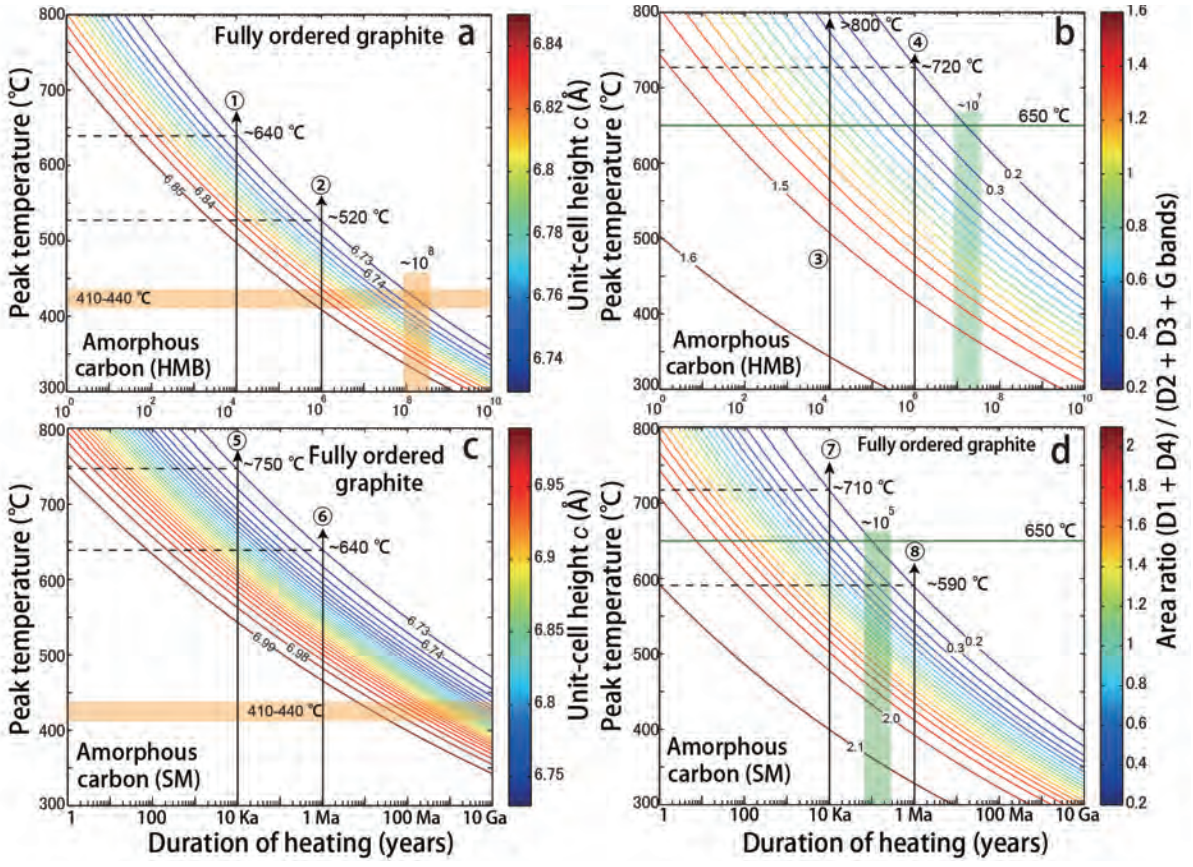

FIGURE 11. Time–temperature–transformation diagram of HMB (**a**) and SM samples (**c**) using the unit-cell height *c* (Å). Orange area indicates the first appearance of fully ordered graphite (d_{002} spacing ~3.36 Å) as reported by Wang (1989). Numerals indicate the unit-cell height *c* (Å), which is contoured at an interval of 0.01 Å. Time–temperature–transformation diagram of HMB (**b**) and SM samples (**d**) using the area ratio of (D1+D4 bands)/(D2+D3+G bands). Numerals indicate the area ratio, which is contoured at an interval of 0.1. Green area indicates the range of intersection at 650 °C. (Color online.)

results and natural graphitization in metamorphic rocks. It can be deduced that the actual activation energies for natural graphitization could be even slightly lower than that estimated here due to the influence of other factors (e.g., catalytic effects, tectonic deformation and fluid activity), and further experiments will help to constrain the influence of additional factors to refine our kinetic model for natural graphitization.

ACKNOWLEDGMENTS

We thank H. Hara for guiding and sampling the pelitic rocks in Shimanto accretionary complex, Central Shikoku, Japan, and H. Konishi for assistance with the TEM observations. We express our special thanks to the colleagues at Niigata University, and C. Zhao, N. Tsujino, D. Yamazaki, A. Yoneda, and E. Ito at IPM, Okayama University for their helps and valuable discussions. The authors acknowledge Laurence Garvie, Ralf Milke, two anonymous reviewers, and Keith Putirka, Joshua Feinberg, and Daniel Hummer for the valuable comments, which have greatly improved the earlier versions of the manuscript. This paper presents a result of a joint research program carried out at the Institute for Planetary Materials, Okayama University. Finally, this work was financially supported by Grant-in-Aid for JSPS Fellows (26-3941). M.S.-K. acknowledges the partial support by JSPS KAKENHI Grant Numbers (JP25302008 and JP15H05831).

REFERENCES CITED

Aoki, K., Maruyama, S., Isozaki, Y., Otoh, S., and Yanai, S. (2011) Recognition of the Shimanto HP metamorphic belt within the traditional Sanbagawa HP metamorphic belt: New perspectives of the Cretaceous–Paleogene tectonics in Japan. Journal of Asian Earth Sciences, 42, 355–369. doi:10.1016/j.jseaes.2011.05.001.

Aoya, M., Kouketsu, Y., Endo, S., Shimizu, H., Mizukami, T., Nakamura, D., and Wallis, S. (2010) Extending the applicability of the Raman carbonaceous-material geothermometer using data from contact metamorphic rocks. Journal of Metamorphic Geology, 28, 895–914. http://doi.wiley.com/10.1111/j.1525-1314.2010.00896.x

Beyssac, O., Goffé, B., Chopin, C., and Rouzaud, J.N. (2002) Raman spectra of carbonaceous material in metasediments: a new geothermometer. Journal of Metamorphic Geology, 20, 859–871. http://doi.wiley.com/10.1046/j.1525-1314.2002.00408.x

Beyssac, O., Brunet, F., Petitet, J.-P., Goffé, B., and Rouzaud, J.-N. (2003) Experimental study of the microtextural and structural transformations of carbonaceous materials under pressure and temperature. European Journal of Mineralogy, 15, 937–951. http://dx.doi.org/10.1127/0935-1221/2003/0015-0937.

Burnham, A.K., and Sweeney, J.J. (1989) A chemical kinetic model of vitrinite maturation and reflectance. Geochimica et Cosmochimica Acta, 53, 2649–2657. doi:10.1016/0016-7037(89)90136-1.

Buseck, P.R., and Beyssac, O. (2014) From organic matter to graphite: Graphitization. Elements, 10, 421–426. DOI: 10.2113/gselements.10.6.421.

Buseck, P.R., and Huang, B.-J. (1985) Conversion of carbonaceous material to graphite during metamorphism. Geochimica et Cosmochimica Acta, 49, 2003–2016. doi:10.1016/0016-7037(85)90059-6.

Bustin, R.M., Rouzaud, J.-N., and Ross, J.V. (1995) Natural graphitization of anthracite: Experimental considerations. Carbon, 33, 679–691. doi:10.1016/0008-6223(94)00155-S.

Charon, E., Rouzaud, J.-N., and Aléon, J. (2014) Graphitization at low temperatures (600–1200 °C) in the presence of iron implications in planetology. Carbon, 66, 178–190. doi:10.1016/j.carbon.2013.08.056.

Cody, G.D., Alexander, C.M.O.D., Yabuta, H., Kilcoyne, a L.D., Araki, T., Ade, H., Dera, P.K., Fogel, M.L., Militzer, B., and Mysen, B.O. (2008) Organic thermometry for chondritic parent bodies. Earth and Planetary Science Letters, 272, 446–455. doi:10.1016/j.epsl.2008.05.008.

Cuesta, A., Dhamelincourt, P., Laureyns, J., Martínez-Alonso, A., and Tascón, J.M.D. (1994) Raman microprobe studies on carbon materials. Carbon, 32, 1523–1532. doi:10.1016/0008-6223(94)90148-1.

Dippel, B., and Heintzenberg, J. (1999) Soot characterization in atmospheric particles from different sources by NIR FT Raman spectroscopy. Journal of Aerosol Science, 30, S907–S908. doi:10.1016/S0021-8502(99)80464-9.

Durand, B., and Nicaise, G., (1980) Procedures of kerogen isolation. In B. Durand, Ed., Kerogen, Insoluble Organic Matter from Sedimentary Rocks. 35–53 p. Editions Techiq, Paris.

Feng, B., Bhatia, S.K., and Barry, J.C. (2002) Structural ordering of coal char during heat treatment and its impact on reactivity. Carbon, 40, 481–496. doi:10.1016/S0008-6223(01)00137-3.

Fischbach, D.B. (1963) Kinetics of graphitization of a petroleum coke. Nature, 200, 1281–1283. doi:10.1038/2001281a0.

——— (1971) The kinetics and mechanism of graphitization. In P.L. Walker, Ed., Chemistry and Physics of Carbon, 7, p. 1–154. Marcel Dekker, New York.

Fujimoto, H. (2003) Theoretical X-ray scattering intensity of carbons with turbostratic stacking and AB stacking structures. Carbon, 41, 1585–1592. doi:10.1016/S0008-6223(03)00116-7.

Grew, E.G. (1974) Carbonaceous material in some metamorphic rocks of New England and other areas. The Journal of Geology, 82, 50–73. http://www.jstor.org/stable/30068626.

Hanfland, M., Beister, H., and Syassen, K. (1989) Graphite under pressure: Equation of state and first-order Raman modes. Physical Review B, 39, 12598–12603. http://dx.doi.org/10.1103/PhysRevB.39.12598.

Hilchie, L.J., and Jamieson, R.A. (2014) Graphite thermometry in a low-pressure contact aureole, Halifax, Nova Scotia. Lithos, 208-209, 21–33. doi:10.1016/j.lithos.2014.08.015.

Hood, A., Gutjahr, C.C.M., and Heacock, R.L. (1975) Organic metamorphism and the generation of petroleum. AAPG Bulletin, 59, 986–996.

Huang, W.-L. (1996) Experimental study of vitrinite maturation: effects of temperature, time, pressure, water, and hydrogen index. Organic Geochemistry, 24, 233–241. doi:10.1016/0146-6380(96)00032-0.

Inagaki, M. (1996) Carbon materials structure, texture and intercalation. Solid State Ionics, 86-88, 833–839. doi:10.1016/0167-2738(96)00337-2.

Inagaki, M., and Meyer, R.A. (1999) Stress graphitization. In P.A. Thrower and L.R. Radovic, Eds., Chemistry and Physics of Carbon, 26, p. 149–244. Marcel Dekker, New York.

Inagaki, M., Murase, Y., and Noda, T. (1968) Effect of pre-heat-treatment on kinetics of graphitization. Journal of the Ceramic Association, Japan, 76, 184–189. http://doi.org/10.2109/jcersj1950.76.874_184 (in Japanese with English abstract).

Itaya, T. (1981) Carbonaceous material in pelitic schists of the Sanbagawa metamorphic belt in central Shikoku, Japan. Lithos, 14, 215–224. doi:10.1016/0024-4937(81)90043-8.

———(1985) Rapid separation technique of carbonaceous materials from a lot of metasedimentary rocks. Bulletin of the Hiruzen Research Institute, Okayama University of Science 11, 47–57 (in Japanese with English abstract).

Iwashita, N., Park, C.R., Fujimoto, H., Shiraishi, M., and Inagaki, M. (2004) Specification for a standard procedure of X-ray diffraction measurements on carbon materials. Carbon, 42, 701–714. doi:10.1016/j.carbon.2004.02.008.

Kanter, M.A. (1957) Diffusion of carbon atoms in natural graphite crystals. Physical Review, 107, 655–663. http://dx.doi.org/10.1103/PhysRev.107.655.

Kaxiras, E., and Pandey, K. (1988) Energetics of defects and diffusion mechanisms in graphite. Physical Review Letters, 61, 2693–2696. http://dx.doi.org/10.1103/PhysRevLett.61.2693.

Kebukawa, Y., Nakashima, S., and Zolensky, M.E. (2010) Kinetics of organic matter degradation in the Murchison meteorite for the evaluation of parent-body temperature history. Meteoritics and Planetary Science, 45, 101–115. http://doi.wiley.com/10.1111/j.1945-5100.2009.01008.x.

Khawam, A., and Flanagan, D.R. (2006) Solid-state kinetic models: Basics and mathematical fundamentals. The Journal of Physical Chemistry B, 110, 17315–17328. doi:10.1021/jp062746a.

Kouketsu, Y., Mizukami, T., Mori, H., Endo, S., Aoya, M., Hara, H., Nakamura, D., and Wallis, S. (2014) A new approach to develop the Raman carbonaceous material geothermometer for low-grade metamorphism using peak width. Island Arc, 23, 33–50. http://doi.wiley.com/10.1111/iar.12057.

Larsen, J.W., Pan, C.S., and Shawver, S. (1989) Effect of demineralization on the macromolecular structure of coals. Energy & Fuels, 3, 557–561. doi:10.1021/ef00017a004.

Luque, F.J., Pasteris, J.D., Wopenka, B., Rodas, M., and Barrenechea, J.F. (1998) Natural fluid deposited graphite: Mineralogical characteristics and mechanism of formation. American Journal of Science, 298, 471–498.

Lynch, R.W., and Drickamer, H.G. (1966) Effect of high pressure on the lattice parameter of diamond, graphite, and hexagonal boron nitride. The Journal of Chemical Physics, 44, 181–184.

Marsh, H., Crawford, D., and Taylor, D.W. (1983) Catalytic graphitization by iron of isotropic carbon from polyfurfuryl alcohol, 725–1090 K. A high resolution electron microscope study. Carbon, 21, 81–87. doi:10.1016/0008-6223(83)90160-4.

Marsh, H., Martínez-Escandell, M., and Rodríguez-Reinoso, F. (1999) Semicokes from pitch pyrolysis: mechanisms and kinetics. Carbon, 37, 363–390. doi:10.1016/S0008-6223(98)00205-X.

Muirhead, D.K., Parnell, J., Taylor, C., and Bowden, S.A. (2012) A kinetic model for the thermal evolution of sedimentary and meteoritic organic carbon using Raman spectroscopy. Journal of Analytical and Applied Pyrolysis, 96, 153–161. doi:10.1016/j.jaap.2012.03.017.

Murty, H.N., Biederman, D.L., Heintz, E.A. (1969) Kinetics of Graphitization—I. Activation energies. Carbon, 7, 667–681. http://dx.doi.org/10.1016/0008-6223(69)90522-3.

Nakamura, Y., and Akai, J. (2013) Microstructural evolution of carbonaceous material during graphitization in the Gyoja-yama contact aureole: HRTEM, XRD and Raman spectroscopic study. Journal of Mineralogical and Petrological Sciences, 108, 131–143. http://doi.org/10.2465/jmps.120625.

Nakamura, Y., Oohashi, K., Toyoshima, T., Satish-Kumar, M., and Akai, J. (2015) Strain-induced amorphization of graphite in fault zones of the Hidaka metamorphic belt, Hokkaido, Japan. Journal of Structural Geology, 72, 142–161. doi:10.1016/j.jsg.2014.10.012.

Noda, T., Inagaki, M., and Sekiya, T. (1965) Kinetic studdies of the graphitization process—I Effect of ambient gas phase on the rate of graphitization. Carbon, 3, 175–180. doi:10.1016/0008-6223(65)90045-X.

Noda, T., Kamiya, K., and Inagaki, M. (1968) Effect of pressure on graphitization of carbon. I. Heat treatment of soft carbon under 1, 3 and 5 kbar. Bulletin of the Chemical Society of Japan, 41, 485–492. http://doi.org/10.1246/bcsj.41.485.

Oberlin, A. (1984) Carbonization and graphitization. Carbon, 22, 521–541. doi:10.1016/0008-6223(84)90086-1.

Oberlin, A., Bonnamy, S., and Rouxhet, P.G. (1999) Colloidal and supermolecular aspect of carbon. In P. A. Thrower and L.R. Radovic, Eds., Chemistry and Physics of Carbon, 26, 1–148 p. Marcel Dekker, New York.

Oberlin, A., Bonnamy, S., and Oshida, K. (2006) Landmarks for graphitization. TANSO, 2006, 281–298. http://doi.org/10.7209/tanso.2006.281.

Ohmori, K., Taira, A., Tokuyama, H., Sakaguchi, A., Okamura, M., and Aihara, A. (1997) Paleothermal structure of the Shimanto accretionary prism, Shikoku, Japan: Role of an out-of-sequence thrust. Geology, 25, 327–330. doi:10.1130/0091-7613(1997).

Rodrigues, S., Suárez-Ruiz, I., Marques, M., Camean, I., and Flores, D. (2011) Microstructural evolution of high temperature treated anthracites of different rank. International Journal of Coal Geology, 87, 204–211. doi:10.1016/j.coal.2011.06.009.

Ross, J.V., and Bustin, R. (1990) The role of strain energy in creep graphitization of anthracite. Nature, 343, 58–60. doi:10.1038/346183a0.

Sadezky, A., Muckenhuber, H., Grothe, H., Niessner, R., and Pöschl, U. (2005) Raman microspectroscopy of soot and related carbonaceous materials: Spectral analysis and structural information. Carbon, 43, 1731–1742. doi:10.1016/j.carbon.2005.02.018.

Schwab, V., Spangenberg, J.E., and Grimalt, J.O. (2005) Chemical and carbon isotopic evolution of hydrocarbons during prograde metamorphism from 100°C to 550°C: Case study in the Liassic black shale formation of Central Swiss Alps. Geochimica et Cosmochimica Acta, 69, 1825–1840. doi:10.1016/j.gca.2004.09.011.

Sheng, C. (2007) Char structure characterised by Raman spectroscopy and its correlations with combustion reactivity. Fuel, 86, 2316–2324. doi:10.1016/j.fuel.2007.01.029.

Sheppard, R.E., Polissar, P.J., and Savage, H.M. (2015) Organic thermal maturity as a proxy for frictional fault heating: Experimental constraints on methylphenanthrene kinetics at earthquake timescales. Geochimica et Cosmochimica Acta, 151, 103–116. doi:10.1016/j.gca.2014.11.020.

Sung, J. (2000) Graphite → diamond transition under high pressure: A kinetics approach. Journal of Materials Science, 35, 6041–6054. doi:10.1023/A:1026779802263.

Sweeney, J., and Burnham, A.K. (1990) Evaluation of a simple model of vitrinite reflectance based on chemical kinetics. AAPG Bulletin, 74, 1559–1570.

Tuinstra, F., and Koenig, L. (1970) Raman spectrum of graphite. The Journal of Chemical Physics, 53, 1126–1130. http://dx.doi.org/10.1063/1.1674108.

Vandenbroucke, M., and Largeau, C. (2007) Kerogen origin, evolution and structure. Organic Geochemistry, 38, 719–833. doi:10.1016/j.orggeochem.2007.01.001.

Wada, H., Tomita, T., Matsuura, K., Iuchi, K., Ito, M., and Morikiyo, T. (1994) Graphitization of carbonaceous matter during metamorphism with references to carbonate and pelitic rocks of contact and regional metamorphisms, Japan. Contributions to Mineralogy and Petrology, 118, 217–228. doi:10.1007/BF00306643.

Wang, G.-F. (1989) Carbonaceous material in the Ryoke metamorphic rocks, Kinki district, Japan. Lithos, 22, 305–316. doi:10.1016/0024-4937(89)90032-7.

Wopenka, B., and Pasteris, J.D. (1993) Structural characterization of kerogens to granulite-facies graphite: Applicability of Raman microprobe spectroscopy. American Mineralogist, 78, 533–557.

Zhao, J., Yang, L., Li, F., Yu, R., and Jin, C. (2009) Structural evolution in the graphitization process of activated carbon by high-pressure sintering. Carbon, 47, 744–751. doi:10.1016/j.carbon.2008.11.006.

Zhou, Q., Xiao, X., Pan, L., and Tian, H. (2014) The relationship between micro-Raman spectral parameters and reflectance of solid bitumen. International Journal of Coal Geology, 121, 19–25. doi:10.1016/j.coal.2013.10.013.

Manuscript received February 24, 2016
Manuscript accepted July 25, 2016
Manuscript handled by Daniel Hummer